journal

J. Am. Ceram. Soc., 98 [10] 2933–2947 (2015)
DOI: 10.1111/jace.13814

Multi-Scale Effects in the Strength of Ceramics

Robert F. Cook†

Materials Measurement Science Division, National Institute of Standards and Technology, Gaithersburg, Maryland 20899

Multiple length-scale effects are demonstrated in indentation-strength measurements of a range of ceramic materials under inert and reactive conditions. Meso-scale effects associated with flaw disruption by lateral cracking at large indentation loads are shown to increase strengths above the ideal indentation response. Micro-scale effects associated with toughening by microstructural restraints at small indentation loads are shown to decrease strengths below the ideal response. A combined meso-micro-scale analysis is developed that describes ceramic inert strength behaviors over the complete indentation flaw size range. Nano-scale effects associated with chemical equilibria and crack velocity thresholds are shown to lead to invariant minimum strengths at slow applied stressing rates under reactive conditions. A combined meso-micro-nano-scale analysis is developed that describes the full range of reactive and inert strength behaviors as a function of indentation load and applied stressing rate. Applications of the multi-scale analysis are demonstrated for materials design, materials selection, toughness determination, crack velocity determination, bond rupture parameter determination, and prediction of reactive strengths. The measurements and analysis provide strong support for the existence of sharp crack tips in ceramics such that the nano-scale mechanisms of discrete bond rupture are separate from the larger scale crack driving force mechanics characterized by continuum-based stress-intensity factors.

I. Introduction

This paper is an edited version of the 2014 Robert B. Sosman (Panel A) Memorial lecture, presented at the 116th Annual Meeting of the American Ceramic Society, October 2014. The paper provides a retrospective on over 30 yr of advances in the understanding of fracture of ceramics—and in particular of the intertwined factors that control the *strength* of ceramics at multiple length scales. Inspiration for the theme of the lecture and paper came from several previous Sosman lectures.

In his 2008 Sosman lecture,[1] Prof. M.P. Harmer posed the question "Interfacial Kinetic Engineering: How Far Have We Come Since Kingery's Inaugural Sosman Address?" Prof. Harmer noted that it was 35 yr since Prof. W.D. Kingery had given the first Sosman lecture[2] (given, coincidentally, the first year of Prof. Harmer's career in ceramics at the University of Leeds), in which Prof. Kingery had discussed "Plausible Concepts Necessary and Sufficient for Interpretation of Ceramic Grain-Boundary Phenomena ….." The focus of Prof. Harmer's lecture and paper was to re-examine the current understanding of grain boundaries in ceramics, in light of the many new grain-boundary observational techniques developed in the intervening 35 yr.

In an analogous fashion, the lecture and paper here will also draw inspiration from a prior Sosman address: The 1982 Sosman lecture was given by Dr. B.R. Lawn on the "Physics of Fracture," which was the second year of my career in fracture, at the University of New South Wales. In his lecture,[3] Dr. Lawn examined the "underlying bases of present-day fracture theory," and proposed that the "atomically sharp crack should be taken as the cornerstone for modeling [crack] propagation." In the 32 yr since Dr. Lawn gave his Sosman lecture, many new ceramic fracture phenomena have been observed, and it seems appropriate to re-examine the implications of the atomically sharp crack concept in modeling these phenomena. The intent of this paper is thus to explore an *application* of the physics of fracture, and a subtitle might be "Strength of Ceramics: How Far Have We Come Since Lawn's Sosman Address?"

The major piece of evidence presented by Lawn in support of the contention that cracks in ceramics and other brittle materials are atomically sharp was the transmission electron microscope (TEM) images of Hockey.[4,5] In these images, the cracks certainly appear sharp in cross section down to the near-nanometer resolution of the images and there does not appear to be any evidence of large-scale deformation, carried by crack tip generated dislocations, say, surrounding the cracks. Perhaps, more telling are the images in plan view, which show Moiré fringes formed in the crack planes, attesting to the near-atomic registry across those planes. The implication of these observations (and many others since) is that cracks in ceramics are atomically sharp such that the bond rupture process is localized to a zone of a few atomic bonds at a well-defined crack tip. The follow-on implication is that the mechanisms and mechanics of fracture are separable. "Mechanisms" here is taken to refer to the "how" of fracture, and specifically that cracks in ceramics propagate by the local, sequential, rupture of discrete interatomic bonds. "Mechanics" here is taken to refer to the "why" of

D. J. Green—contributing editor

Manuscript No. 36968. Received May 28, 2015; approved July 7, 2015.
†Author to whom correspondence should be addressed. e-mail: robert.cook@nist.gov

Feature

fracture, and specifically that stress fields around crack tips in ceramics are independent of the bond rupture mechanisms, and are well described by linear-elastic continuum mechanics. Mechanisms were the focus of the paper by Lawn[3] and the localized, bond rupture process was the "physics of fracture" of the title. Mechanics is the focus here, and the delocalized, linear, stress field surrounding the crack tip—a key implication of this physics of fracture—will be seen to be a key enabler in developing quantitative models for ceramic strength.

Models of cracks in materials under applied stress that incorporate interatomic or interplanar force-displacement laws, whether discrete[6] or continuous,[7] are consistent with the TEM observations. Such models use the force law to self-consistently calculate a crack opening profile and the material stress field to match the far-field boundary conditions. In the body of the material far ahead of the crack tip the stress field approaches that of the far-field, the atoms or planes are at near equilibrium separation, and the bonds are deformed in a linear force-displacement range. As the crack tip is approached the stress increases, until right at the "tip" the stress reaches a maximum, the strength of the bond. Immediately behind the tip the stress rapidly decreases, reaching zero some distance behind the crack tip in the crack opening. The nonlinear force-displacement tip region, where the stress passes through a maximum and then decreases to zero, is extremely small, at most a few interatomic spacings.[6,7] In fact, the vast majority of the stress field surrounding the crack is described by linear-elastic continuum analyses for a cracked body, which, of course, take no account of details of crack tip bond rupture mechanisms. In particular, all components of stress, σ, surrounding the crack in the body are given by $\sigma = K/(2\pi r)^{1/2}$, where r is a radial coordinate measured from the crack tip; this decaying $r^{-1/2}$ stress field pertains in the body for distances thousands of times larger than the localized nonlinear tip region. The amplitude of this field is the stress-intensity factor (SIF), K. The importance of SIFs is that they are determined by the mechanics of external loading conditions,[8] independent of fracture mechanisms (and environment) at the crack tip. (Remote from the crack, the stress approaches the applied stress and the SIF does not apply; the mechanics of fracture is concerned with stress fields surrounding the crack.)

The specific goal of this paper is to apply the SIF formalism to three real-world ceramic strength phenomena at multiple length scales. These phenomena, hints of which were becoming apparent in my early research with Lawn in 1982, are as follows:

1. Large contacts are different from small contacts—the lateral crack problem (meso-scale).
2. Long cracks are different from short cracks—the microstructure problem (micro-scale).
3. Rapid loading is different from slow loading—the environment problem (nano-scale).

The descriptors following the phenomena give the colloquial terms for the (now identified) causes of the phenomena and the fracture mechanics problems required to be solved to model ceramic strength. The length scales over which the phenomena act are given in parentheses and are hundreds of micrometers or larger (meso), one to one hundred micrometers (micro), and nanometers or smaller (nano). The first two of these are equilibrium fracture phenomena and the third is a nonequilibrium (or kinetic) phenomenon. The fracture system to be used as the test vehicle displaying these phenomena is the indentation-strength methodology. This methodology involves a two-step sequence, Fig. 1: (1) A sharp indenter is loaded onto a ceramic sample surface with a prescribed peak contact load. The indentation contact generates a localized zone of plastic deformation with an attendant residual stress field in the surrounding elastically deformed matrix. The stress field initiates cracks from nuclei formed in the plastic deformation zone and stably propagates these cracks into the elastic matrix. (2) The sample is loaded, usually in bending to avoid the gripping issues associated with brittle materials in tension, and the maximum sustainable applied stress, the sample strength, is measured. The tensile applied stress field unstably propagates the indentation cracks, which, if large enough, thus control the strength. The advantage of this methodology is that the size and location of the "indentation flaw" can easily be controlled and thus the fracture mechanics of the system can be well posed in terms of the residual and applied stress fields. Indentation-strength measurements can thus be interpreted in terms of the three phenomena listed above.

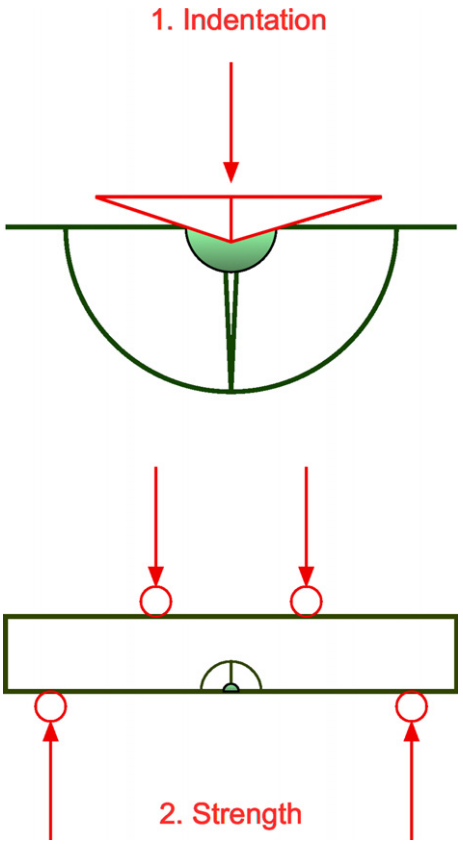

Fig. 1. Schematic diagram of fracture properties measurement by the sequential indentation-strength methodology: 1. Semicircular half-penny cracks are generated in the surface of a brittle material test specimen by indentation to a controlled peak load with a pyramidal indenter. The cracks are initiated within a localized plastic deformation zone formed beneath the indenter and propagated to stable equilibrium lengths in a residual stress field in the surrounding elastically deformed matrix; 2. The indentation flaw is placed in tension, typically by bending the test specimen, and the stress required to unstably propagate the cracks, the strength, is measured.

Section II of this paper will give the background and analyses, developed since 1982,[9,10] for interpreting indentation-strength measurements including the three phenomena. The section will first develop and apply mechanics analyses to describe equilibrium indentation-strength phenomena at the meso- and micro-scales, and tie these two together in a single formulation. This section will then develop and apply an analysis to describe nonequilibrium indentation-strength behavior, originating from phenomenon at the nano-scale and finally tie the three length scales together in a single formulation. Section III will apply these analyses to indentation-strength measurements on a range of ceramic materials, some published,[10–14] illustrating the diversity of responses. Section IV will include applications of these analyses. Section V will offer some conclusions to be drawn from the results of Sections III and IV.

II. Multi-Length-Scale Models for Fracture

(1) Ideal Indentation Fracture

Figure 2(a) shows a schematic plan view of an ideal indentation flaw, formed in a ceramic surface by a four-sided pyramidal Vickers indenter, after indenter unloading and removal. At the center of the flaw is a square residual contact impression of diagonal $2a$; the impression lies within a nearly hemispherical zone of localized plastic deformation with diameter also approximately $2a$, shown in the schematic cross-sectional view of Fig. 1. The mean supported contact stress during the formation of such an impression is $P/2a^2$, where P is the peak indentation load. Material resistance to such contact plastic deformation is the hardness, H. Equating the stress and the hardness and inverting gives the relationship between the contact impression dimension and the indentation load:

$$a = (P/2H)^{1/2} \tag{1}$$

The contact behavior of many ceramic materials is well described by Eq. (1) over indentation load ranges of several orders of magnitude,[9,14] representing invariant hardness in these ranges.

The zone of plastically deformed material remains compressed after indentation, leading to a residual stress field in the surrounding elastic matrix that can lead to fracture.[15,16] In particular, the residual field includes circumferential tension at the material surface exterior to the plastic deformation zone. A consequence is that, above "threshold" indentation loads,[16,17] cracks can initiate from fracture nuclei formed in the plastic deformation zone and propagate stably into the surrounding elastic matrix. Functionally, for Vickers indentations, "radial" cracks initiate at the surface near the contact impression corners and propagate away from the impression, perpendicular to the surface. As the load is increased the cracks also propagate into the depth of the material and may coalesce beneath the plastic deformation zone to form two perpendicular near semi-circular "half-penny" cracks. The surface traces of such cracks are shown in the schematic plan view of Fig. 2(a) and the cross sections are shown in Fig. 1. The SIF for the half-penny cracks in the residual indentation stress field, K_r, is well described by the form of that for an imbedded, center-loaded circular crack,[15,18]

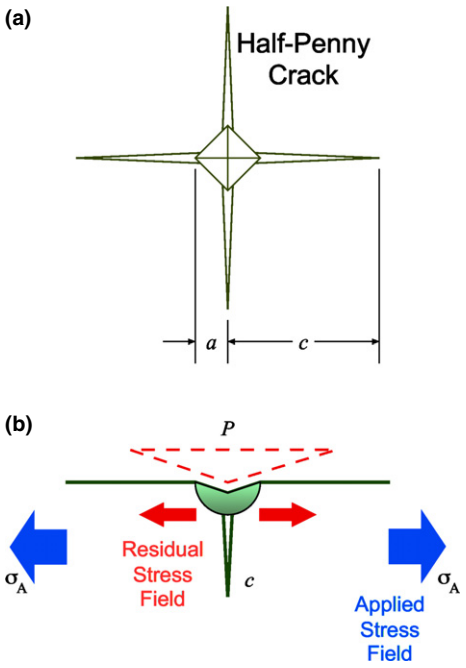

Fig. 2. (a) Schematic plan-view diagram of an ideal Vickers indentation flaw in a ceramic showing the dimensions of the square plastic deformation surface impression and the cross-shaped surface traces of the half-penny cracks. (b) Schematic section-view diagram of an ideal indentation flaw during an indentation-strength test. The hemispherical plastic deformation zone imbedded in the surrounding elastic matrix generates a localized residual stress field. The remote tension provides a uniform applied stress field. During the test, both the residual and applied fields provide crack driving forces.

$$K_r = \chi P/c^{3/2} \tag{2}$$

where c is the crack length measured from the contact impression center, Fig. 2(a), and χ is a (material-dependent) dimensionless constant taking into account surface- and crack geometry-effects as well as the amplitude of the residual stress field. The SIF is the driving force for fracture (just as the mean supported contact stress was that for plastic deformation). The material property characterizing the resistance to fracture is the toughness, T. Equating the SIF and the toughness, $K_r = T$, gives the variation of the equilibrium half-penny crack length, c_0, with indentation load:

$$c_0 = (\chi P/T)^{2/3} \tag{3}$$

The equilibrium is stable as any positive perturbation in c_0 leads to $K_r < T$. The indentation crack lengths of many ceramic materials are well described by Eq. (3), again over several orders of magnitude of indentation load,[9,14,19] although some care must be taken in interpreting such observations: The value of χ and the variation of T with crack length are not known with nearly the same confidence as the geometry of the plastic deformation zone and H. In the absence of other information, such descriptions strictly point to the invariance in T/χ over the indentation load range. If χ is known then the inferred single-valued toughness is that for the environment in which the cracks propagated (in most cases moisture-containing air).

Figure 2(b) shows a schematic cross section of an ideal indentation flaw in a ceramic sample during an indentation-strength test. The localized residual stress field acting on the crack is indicated by the small arrows. The remotely applied uniform tensile stress, σ_A, is indicated by the large arrows. The SIF for the applied stress, K_a, is

$$K_a = \psi \sigma_A c^{1/2} \tag{4}$$

where ψ is a dimensionless crack geometry term. Equation (4) differs from Eq. (2) in a very important respect: Whereas the SIF in Eq. (2) represents a stabilizing fracture field, $dK_r/dc < 0$, that from Eq. (4) represents a destabilizing fracture field, $dK_a/dc > 0$, with the implication that if the magnitude of the applied stress is made great enough, the fracture system will become unstable and any positive perturbation in c will lead to unrestrained crack extension; the magnitude of the stress at which this occurs is thus the sample strength. If such fracture occurs in the absence of any reactive species, that is if the environment is inert (*e.g.*, dry N_2 gas or silicone oil), the strength is the "inert strength." The net SIF, K, acting on the indentation flaw represented in Fig. 2(b) is

$$K = K_a + K_r = \psi \sigma_A c^{1/2} + \chi P/c^{3/2} \tag{5}$$

and the equilibrium condition is $K = T_0$, where T_0 is the material toughness in an inert environment and a maximum for a material. As the applied and residual SIFs have opposing stability effects, the strength, σ_{max}, is found by simultaneously

solving the equilibrium equation and the equation describing incipient instability, $dK/dc = dT_0/dc = 0$, to give[20]

$$\sigma_{max} = \frac{3T_0^{4/3}}{4^{4/3}\psi\chi^{1/3}P^{1/3}} \quad (6)$$

Many ceramic materials are well described by Eq. (6), but again some care must be taken in interpretation: The values and variations of χ and ψ with indentation load and the variation of T_0 with crack length are not known *a priori* in the absence of other information, and such descriptions strictly point to the invariance in $(T_0^{4/3}/\psi\chi^{1/3})$ over indentation load ranges usually more restricted than those for indentation dimensions described by Eqs. (1) and (3). If the geometry parameters are known to be invariant then the inferred single-valued toughness is that for an inert environment.

Many ceramic materials do not exhibit indentation-strength behavior described by Eq. 6, particularly when the range of indentation loads is large [even if Eqs. (1) and (3) appear to describe indentation observations] or if the microstructural scale is large. In these cases, the ideal indentation-strength analysis must be modified to take account of meso- and micro-scale phenomena.

(2) Meso-Scale Phenomena

In addition to the component of the residual stress field driving the half-penny cracks, there is a component of radial tension in the body of the material beneath the plastic deformation zone. A consequence is that, above threshold indentation loads somewhat greater than those for radial and half-penny crack initiation, "lateral" cracks can initiate from fracture nuclei at or near the base of the plastic deformation zone and propagate stably into the surrounding elastic matrix parallel to the surface.[16,21] As the load is increased the cracks turn and propagate toward the surface and may eventually reach the surface, removing a chip of material. A consequence is that for indentation loads greater than the lateral crack threshold, the plastic deformation zone is increasingly decoupled from the surrounding constraining material and the residual field in the elastic matrix is decreased, Fig. 3(a). The reduction in the residual field due

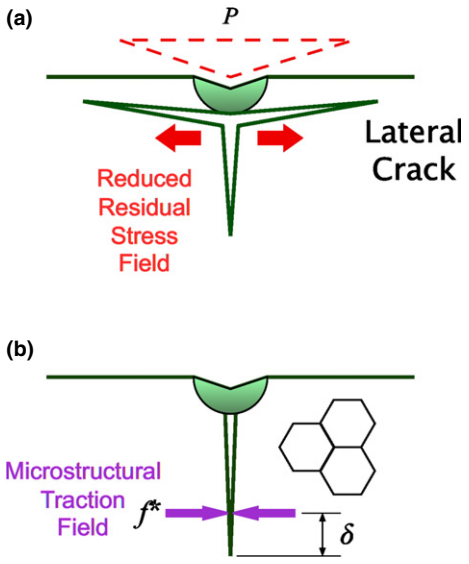

Fig. 3. Schematic diagrams of phenomena that provide deviations from ideal indentation behavior. (a) At the meso-scale, lateral cracks initiated beneath the plastic deformation zone and propagating parallel to the surface decouple the zone from the surrounding material and reduce the residual stress field. (b) At the micro-scale, microstructural interactions generate a restraining field behind the crack tip that acts to oppose crack opening and crack extension.

to this meso-scale phenomenon at the scale of the flaw is described by a modification to Eq. (2) and an additional load-dependence for the residual SIF:[22]

$$K_r = \frac{\chi}{(1 + P/P_L)}\frac{P}{c^{3/2}} \quad (7)$$

where P_L is a characteristic indentation load at which lateral crack effects become significant. P_L is related via the modulus and hardness of the material to the physical increase in volume provided by the lateral cracks for the compressed plastic deformation zone.[22] The inert strength is then given by

$$\sigma_{max} = \sigma_L(1 + P_L/P)^{1/3} \quad (8a)$$

where

$$\sigma_L = \frac{3T_0^{4/3}}{4^{4/3}\psi\chi^{1/3}P_L^{1/3}} \quad (8b)$$

is a characteristic strength. For small indentation loads, $P << P_L$, the strength given by Eq. (8a) tends asymptotically to the ideal strength given by Eq. (6). For large indentation loads, $P >> P_L$, the strength tends asymptotically to the invariant strength minimum given by Eq. (8b); in this range increased indentation loads do not lead to increased residual fields.

(3) Micro-Scale Phenomena

In many ceramic materials, propagating cracks interact significantly with the material microstructure. Polycrystalline alumina (Al_2O_3) has been particularly well studied in this regard and perhaps best exemplifies the combined effects on fracture of (nontransforming) ceramics of weak grain boundaries, elastic and fracture anisotropy of grains, and inhomogeneous thermally generated stress fields. The relevant observations date back to Coble (as cited in Kingery et al.[23]), and particularly include those by Steinbrech,[24] Swain,[25] Lawn and Bennison,[26,27] and their coworkers. Al_2O_3 crystals exhibit thermal expansion anisotropy and as a consequence polycrystalline Al_2O_3 develops thermal expansion stress fields on cooling from the processing temperature;[28] if the grain size is large enough, the stresses are large enough to initiate thermal microcracks in the material.[27] Long crack propagation in polycrystalline Al_2O_3 is predominantly intergranular;[23,25] the fracture traces frequently exhibit discontinuities; and the fracture resistance is greater than that of single crystal Al_2O_3 (sapphire).[23,26,27] Strength test samples of polycrystalline Al_2O_3 containing short indentation cracks often exhibit retained strength after testing; observations of such fractured samples show grain-localized restraints holding the cracks and the sample together.[29] These crack wake restraints fall into two main categories: (i) ligamentary (cantilever) bridges formed by discontinuous crack propagation and (ii) frictional (shear) interlocks formed by crack propagation perpendicular to the predominant fracture direction. These restraints remain intact in a zone behind the crack tip, where the crack opening displacement is small, and ruptured behind this zone, where the crack opening displacement is large. In summary, crack propagation in polycrystalline Al_2O_3 proceeds mostly along grain boundaries but sometimes, under the combined effects of thermal expansion stress fields and elastic and fracture anisotropy, a ligamentary or shear restraint forms that acts against local crack opening. If the crack becomes long enough, the crack opening displacements furthest from the crack tip are large enough to rupture restraints and a near steady-state zone of active restraints propagates behind the crack tip. The scale of the restraints,

their separation, and the scale of the steady-state zone are all determined by the microstructure. Similar observations have been made for many other materials.

A model for the microstructural traction field of restraints is shown in the schematic diagram of Fig. 3(b). The zone of restraints is represented by a line-force of magnitude f^* acting a characteristic fixed distance δ behind the crack tip; for the cross section of the half-penny indentation crack shown in Fig. 3(b), the line-force extends over a semicircle. The SIF for this configuration, characterizing micro-scale phenomena at the scale of the microstructure, illustrated schematically in Fig. 3(b), is given by[9]

$$K_\mu = -\mu f* \delta^{-1/2}[1 - (\delta/c)^{3/2}],\ c \geq \delta \tag{9}$$

where μ is a microstructural geometry factor and the minus sign serves to emphasize that K_μ opposes crack propagation. The net SIF for an indentation flaw under applied stress in such a microstructural field is given by extending Eq. (5),

$$\begin{aligned} K &= K_a + K_r + K_\mu \\ &= \psi\sigma_A c^{1/2} + \chi P/c^{3/2} - \mu f^* \delta^{-1/2}[1 - (\delta/c)^{3/2}] \end{aligned} \tag{10}$$

and it can be seen that the effect of the microstructure is a stabilizing fracture field, $dK_\mu/dc < 0$. Once again, the inert strength is found by simultaneously solving the equilibrium and incipient instability equations to give

$$\sigma_{max} = \sigma_\mu(1 + P/P^*)^{-1/3} \tag{11a}$$

where

$$\sigma_\mu = \frac{3T_\infty^{4/3}}{4^{4/3}\psi(\chi P^*)^{1/3}} \tag{11b}$$

is a characteristic strength, and

$$P^* = \mu f^* \delta/\chi \tag{12a}$$

$$T_\infty = T_0 + \Delta T \tag{12b}$$

$$\Delta T = \mu f^* \delta^{-1/2} \tag{12c}$$

For large indentation loads, $P >> P^*$, the strength given by Eq. (11a) tends asymptotically to the ideal strength given by Eq. (6). For small indentation loads, $P << P^*$, the strength tends asymptotically to the invariant strength maximum given by Eq. (11b); in this range decreased indentation loads do not lead to decreased crack lengths at instability.

(4) Combined Meso- and Micro-Scale Inert Strength

The inert indentation-strength over the full indentation load range, encompassing both meso- and micro-scale phenomena, is given by[9]

$$\sigma_{max} = \sigma_\mu(1 + \tilde{P}/P^*)^{-1/3} \tag{13a}$$

where

$$\tilde{P} = \frac{PP_L}{(P + P_L)} \tag{13b}$$

is an effective indentation load. The inert strength response given by Eq. (13a) is sigmoidal, passing between two strength asymptotes: At small indentation loads, the strength tends to the upper, microstructural-controlled strength [Eq. (11b)]; at large indentation loads, the strength tends to the lower, lateral crack-controlled strength [Eq. (8b)]. Between these two, the strength passes through the ideal response [Eq. (6)]. An example for a Cr-doped alumina[9] is shown in Fig. 4: The bold solid line is the full meso- plus micro-response [Eq. (13a)], the fine solid lines are the separate meso- and micro-responses [Eqs. (8a) and (11a)], and the dashed line is the ideal response [Eq. (6)].

(5) Nano-Scale Phenomena

Fracture in many ceramic materials, particularly oxides, is significantly influenced by the presence of water (H_2O).[30] A brittle ceramic containing M-O-M bonds, where M is a metal cation, fractured under inert conditions generates surfaces containing M• and M-O• species, where • represents a free radical. The average excess energy per unit area of such surfaces is γ_0, where the 0 subscript represents the inert environment; the fracture surface energy (density) is then $2\gamma_0$. If such a surface is exposed to water, reaction leads to hydrolysis and the formation of M-OH and HO-M surface species. The average excess energy areal density is now $\gamma < \gamma_0$. If the ceramic is fractured under such reactive conditions the reaction

$$\text{M-O-M} + H_2O \rightarrow \text{M-OH} + \text{HO-M} \tag{14}$$

takes place and the fracture energy is 2γ. There are two implications of Eq. (14). The first is that equilibrium fracture strengths [Eqs. (6), (8b), and (11b)] will be smaller in reactive water environments compared with inert environments, reflecting the smaller fracture energy. The second is that there will be an energy barrier separating the initial and final states represented by the chemical reaction of Eq. (14), and hence kinetics will play a role in reactive fracture.

In addressing the equilibrium energetics of such nano-scale fracture phenomena, it is more convenient to characterize the crack driving force by the mechanical energy release rate, $G = -dU_M/dA$, where U_M is the mechanical energy of the fracture system and A is the crack area.[8] The analogous crack resistive force is the fracture resistance, $R = dU_S/dA$, where U_S is the (total) surface energy of the fracture system;

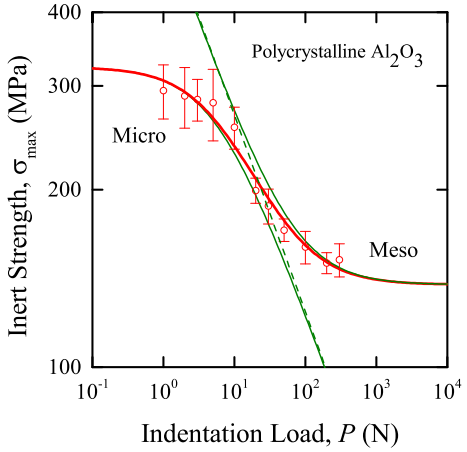

Fig. 4. Plot of the inert indentation-strength response of a large-grained polycrystalline alumina. The symbols represent the means and standard deviations of at least 12 strength measurements at the indentation loads indicated. The bold solid line is the best fit to the measurements using a combined meso-micro-scale fracture model. The fine solid lines are the separate meso- and micro-response asymptotes. The dashed line is the ideal indentation response asymptote.

for the reactive case here, $R = 2\gamma$, and for the inert case, $R = 2\gamma_0$. Fracture equilibrium, for which there is no crack motion, is thus given by $G = 2\gamma$ in the reactive environment and $G = 2\gamma_0$ in the inert environment.[31] The connection between G, characterizing the flux of energy to the crack tip region to break bonds, and K, characterizing the work performed by the external applied loading is given by the Irwin relation:[8]

$$G = K^2/E \tag{15}$$

where E is the Young's modulus of the material (elastic isotropy and plane stress assumed). Comparison of the equilibrium equations in reactive conditions, $G = 2\gamma$ and $K = T$, with the Irwin relation shows that the toughness in the reactive environment is $T = (2\gamma E)^{1/2}$ and comparison with inert conditions gives $T_0 = (2\gamma_0 E)^{1/2} > T$. It is thus possible to define a characteristic strength in the reactive environment, in analogy to that for the inert environment of Eqs. (11a) and (13a), by

$$\sigma_{\min} = \sigma_{\mu,\min}(1 + \tilde{P}/P^*)^{-1/3} \tag{16a}$$

where

$$\sigma_{\mu,\min} = \frac{3T_{\infty,\min}^{4/3}}{4^{4/3}\psi(\chi P^*)^{1/3}} \tag{16b}$$

and

$$T_{\infty,\min} = T + \Delta T \tag{16c}$$

The subscript "min" in Eq. (16a) indicates that the strength is the minimum that can be observed with the specified indentation load. It is a minimum as the surface is assumed to be in full reactive equilibrium; all broken bonds that could react with environmental species have done so. For this to be the case, every reactive bond must have had sufficient time to overcome the energy barrier separating the initial (unbroken) and final (fully reacted) states in Eq. (14). The implication is that $\sigma_{\min}$ is approached at very slow applied stressing rates, such that sufficient time is provided for every bond to react. This is in distinction to the inert strength $\sigma_{\max}$, which is observed when no bond reacts.

Strengths intermediate to $\sigma_{\min}$ and $\sigma_{\max}$ will be observed for applied stressing rates that lead to failure times comparable to those imposed by the kinetics of bond rupture and reaction. Such kinetics are incorporated into a reactive strength formulation by extending the surface energy expression beyond the average value to include a periodic array of energy barriers to bond rupture and reaction:[10,32]

$$U_S = u_0(A/a^2) - (u_1/2)\cos(2\pi A/a^2) \tag{17}$$

where a^2 is the incremental bond area, such that a here is the average separation between barriers or bonds, u_0 is the energy to break a bond and react with the environmental species, and u_1 is the barrier height in fracture equilibrium, $G = 2\gamma$. In equilibrium, the barrier heights for bond rupture and bond healing are identical. Under nonequilibrium conditions, $2\gamma < G < 2\gamma_0$, the barriers for rupture are decreased and the barriers for healing are increased, such that the frequency of rupture becomes greater than that of healing and there is a net increase in crack area. Assuming Arrhenius kinetics and linear dependence of the barrier heights on separation from equilibrium leads to an areal rate of crack extension given by[10,32]

$$\dot{A} = \dot{A}_0 \sinh[(G - 2\gamma)/\eta] \tag{18}$$

where $\dot{A} = dA/dt$ and t is time. The macroscopic crack extension rate terms are related to those of the nano-scale surface energy expression by

$$\eta = 2kT/a^2 \tag{19a}$$

$$2\gamma = u_0/a^2 \tag{19b}$$

$$\dot{A}_0 = 2f_0 a^2 \exp(-u_1/kT) \tag{19c}$$

where k = Boltzmann's constant, here T = temperature, and f_0 is the characteristic frequency for bond rupture and healing in the equilibrium state. The crack velocity, $v = dc/dt$, along a particular dimension c of a crack is given by[10]

$$v = v_0 \sinh[(G - 2\gamma)/\eta]/b \tag{20}$$

where

$$v_0 = 2f_0 a \exp(-u_1/kT) \tag{21a}$$

and

$$b = dA/a dc \tag{21b}$$

For a half-penny crack, $b = 2\pi c/a$. Equation (20) has been shown to be extremely effective in describing indentation crack extension in reactive environments, macroscopic crack growth in reactive environments, including the effects of temperature, and the strengths of ceramics measured under constant stressing rate conditions in water.[10,32] In all cases, a critical feature of the observations has been the appearance of a zero in the crack velocity, $v = 0$, included in Eq. (20) at fracture equilibrium, $G = 2\gamma$: 2γ is thus the *threshold* value for crack propagation.

(6) Combined Meso-, Micro-, and Nano-Scale Reactive Strength

The crack velocity expression, Eq. (20), provides a means of calculating the time, t_f, required for a crack to extend from an initial length, c_i, to a final length, c_f, by the integral[10]

$$t_f = \int_0^{t_f} dt = \int_{c_i}^{c_f} \frac{dc'}{v(G; c', t)} \tag{22}$$

The conditions of interest here are for a ceramic specimen containing an indentation flaw in a reactive water environment exposed to an applied stress increasing linearly with time from zero. In this case the applied stress is given by

$$\sigma_A = \dot{\sigma}_a t \tag{23}$$

where $\dot{\sigma}_a$is the applied stressing rate. The first half of the linkage between the micro- and meso-scale phenomena and the nano-scale phenomena combines the full SIF expression of Eq. (10) with the Irwin relation of Eq. (15) to arrive at the mechanical energy release rate for the ceramic specimen,

$$G = [\psi\dot{\sigma}_a t c^{1/2} + \chi(\tilde{P} + P^*)/c^{3/2} - \Delta T]^2/E \tag{24}$$

using Eqs. (12) and (23). The second half of the meso-micro-nano-scale linkage is to use Eq. (24) in Eq. (20) and thence Eq. (22) to calculate the nonequilibrium extension of the indentation crack. The initial condition for such extension is given by stable equilibrium in the reactive environment under zero stress,

$$[\chi(\tilde{P}+P^*)/c_i^{3/2}-\Delta T]^2/E=2\gamma, \tag{25a}$$

noting that the initial crack length, c_i, may be longer than c_0 of Eq. (3) if T in water is significantly less than T in air and sufficient time is allowed between exposure of the indentation to water and imposition of the applied stress. The final condition for such extension is given by unstable equilibrium in the inert environment at a nonzero stress,

$$[\psi\dot{\sigma}_a t_f c_f^{1/2}+\chi(\tilde{P}+P^*)/c_f^{3/2}-\Delta T]^2/E=2\gamma_0 \tag{25b}$$

recognizing that the nonzero stress is the reactive failure strength of the specimen, σ_f, given by

$$\sigma_f=\dot{\sigma}_a t_f \tag{25c}$$

Experimentally, the meso-micro-nano-linkage is made by first performing inert strength measurements and fitting the full inert strength model to the data to obtain P_L, P^*, and σ_μ. Inversion of the characteristic strength equation then provides T_∞, which allows self-consistent determination[9] of δ and T_0 and thus ΔT; $2\gamma_0$ follows from the Irwin relation (noting that ψ, χ, and E are required). Specification of P and $\dot{\sigma}_a$ used in a subsequent reactive strength test allows the mechanical energy release rate and initial and final conditions for the crack extension integral to be calculated. Selection of the parameters v_0, 2γ, and η enables the integral to be completed, albeit numerically, and the reactive strength determined. Such strengths can then be compared with reactive strength measurements and the crack velocity parameters refined to best fit the data. This experimental sequence is the subject of the next section.

III. Indentation-Strength Measurements

(1) Inert Strengths

Figure 5 is a composite plot of the indentation-strength, $\sigma_{max}(P)$, responses of seven ceramic materials measured under inert conditions. Four of the materials are variants of Al_2O_3: single crystal (sapphire); a polycrystal with about 10% glass by volume (AD90); a polycrystal with about 0.1% glass by volume (AD999); and a glass-free large-grained polycrystal with about 0.1% MgO by atomic fraction (Vistal). The other three materials are a fine-grained glass ceramic (cordierite), a Bi-doped barium titanate (Bi-$BaTiO_3$), and a composite glass ceramic consisting of mica flakes in a glass matrix (Macor). The symbols represent the means and standard deviations of at least ten inert strength measurements at each indicated indentation load. Experimental details are given in Refs. [11] and [14] Table I lists the materials and their associated E and H values.

The solid lines in Fig. 5 represent best fits to the data using the meso-micro-scale strength relation of Eq. (13). The dashed lines in Fig. 5 represent the ideal asymptotic $P^{-1/3}$ responses of Eq. (6). The three non-Al_2O_3 materials exemplify limits of the full strength response: the cordierite exhibits almost ideal response, Eq. (6), over the indentation load range; the Bi-$BaTiO_3$ exhibits meso-scale influence alone on strength, Eq. (8), at large indentation loads; and, the Macor exhibits micro-scale influence alone on strength, Eq. (11), at small indentation loads. The three polycrystalline Al_2O_3 materials exhibit varying levels of simultaneous meso- and micro-scale influences: the AD90 exhibits small meso- and micro-scale combined influences such that only the smallest and largest indentation load data deviate from the ideal response; the AD999 exhibits larger combined influences; and, the Vistal exhibits such large combined influences that none of the data are well described by the ideal response and the best fit passes through the $P^{-1/3}$ asymptote. Sapphire can provide no microstructural influence of course, and exhibits a meso-scale influence alone. Table I gives the parameters σ_μ, σ_L, P^*, and P_L for each material describing the best fit solid lines of Fig. 5 (noting that only three of the four are independent), along with the combination $\sigma_\mu(P^*)^{1/3}=\sigma_L(P_L)^{1/3}$ describing the asymptotic dashed lines.

Table I also gives the values of T_∞ for each material determined using this combination parameter. Extensive measurements have shown that $\psi=1.24$ and $\chi=0.0040(E/H)^{1/2}$ are good estimates for the geometry parameters in indentation-strength tests[33] (but not crack length measurements[19]) and these were the parameters used here. Upper-bound estimates for δ and T_0 were determined from the T_∞ values, and $2\gamma_0$ values were thence determined from the T_0 values, and these additional three values are also given in Table I.

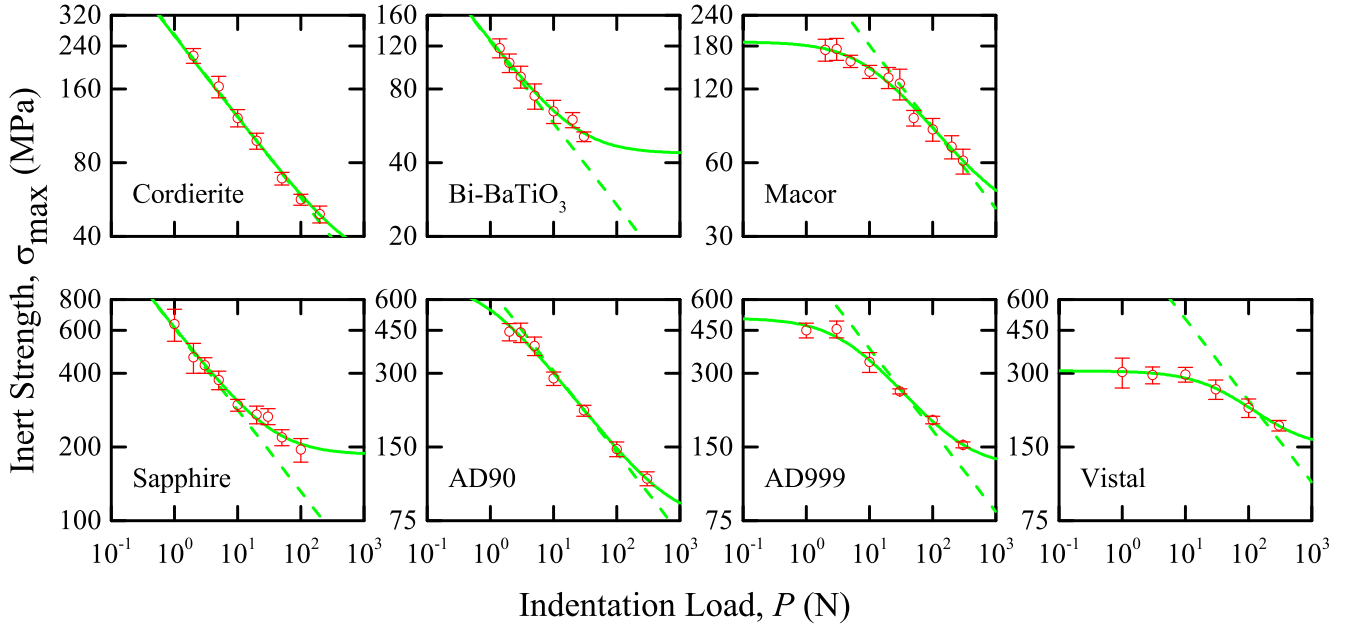

Fig. 5. Plots of the inert indentation-strength responses for a range of ceramic materials. The solid lines represent best fits to the measurements using a combined meso-micro-scale fracture model. The dashed lines represent ideal indentation responses.

Table I. Ceramic Deformation and Inert Fracture Properties

Material	Deformation parameters E (GPa) H (GPa)	Indentation-strength parameters σ_L (MPa) σ_μ (MPa)	 P_L (N) P^* (N)	 $\sigma_L P_L^{1/3}$ (MPa·N$^{1/3}$)	Toughness and fracture resistance parameters T_0 (MPa·m$^{1/2}$)	 T_∞ (MPa·m$^{1/2}$)	 δ (μm)	 $2\gamma_0$ (J/m^2)
Sapphire	425 21.8	186 —	35.4 —	610.7	2.93	—	—	20.2
AD90	276 13.0	74.3 714	701 0.79	660.1	2.81	3.13	12.7	28.6
AD999	386 20.1	124.2 504	283 4.24	815.7	2.31	3.62	14.8	13.9
Vistal	393 19.0	154 307	343 43.2	1077	1.74	4.50	43.2	7.7
Cordierite	134 7.9	29.7 —	700 —	263.7	1.53	—	—	17.5
Bi-$BaTiO_3$	123 7.8	43.6 —	23.5 —	124.9	0.67	—	—	6.1
Macor	64.1 2.0	34.6 187	1428 9.03	389.4	1.44	2.22	41.0	32.3

(2) Reactive Strengths

Figure 6 is a composite plot of the reactive strength, $\sigma_f(\dot{\sigma}_a)$, responses of the seven ceramic materials. The symbols represent the means and standard deviations of at least eight reactive strength measurements at each of the indicated applied stressing rates. Table II lists the materials and the indentation loads used for the measurements. The hatched boxes in the right of the plots are the inert strength mean and standard deviation limits at the indentation load used. Experimental details are given in Refs. [12] and [13].

The solid lines in Fig. 6 represent best fits to the reactive strength data using the meso-micro-nano-scale strength relations and analysis sequence described in the previous section. The fitting method was to calculate σ_f values from solution of the crack extension integral using the experimental applied stressing rates and a three-dimensional matrix of discrete (v_0, 2γ, η) values. The integral was solved numerically using a sixth-order Runge–Kutta algorithm such that relative changes in v between each integration step were less than 0.2%.The sum (over all the stressing rates) of the squared error (SSE) between the calculated and measured σ_f values was determined for each choice of (v_0, 2γ, η). SSE was minimized to provide the best fit between calculated and measured values by (manually) steering the span of the matrix values and reducing their separation. The solid lines in Fig. 6 were obtained using numerical solutions to the integral over the stressing-rate ranges used in the plots and the best fit parameters.

A key feature in Fig. 6 is that at slow stressing rates the measured reactive strengths for all the materials approach invariant minima and these minima were observed over several orders of magnitude of applied stressing rate. These minima correspond to the minimum reactive equilibrium strength σ_{min} of Eq. (16b). Comparison of these minimum strengths with the conjugate applied stressing rates and Eq. (25c) suggests that these fracture surfaces reached chemical equilibrium with the water environment in times of tens of minutes. As the applied stressing rates increased, the reactive strengths increased, approximately logarithmically with stressing rate. Another feature in Fig. 6, common to nearly all the materials, is that at the fastest stressing rates the reactive strengths were less than the inert strengths and still

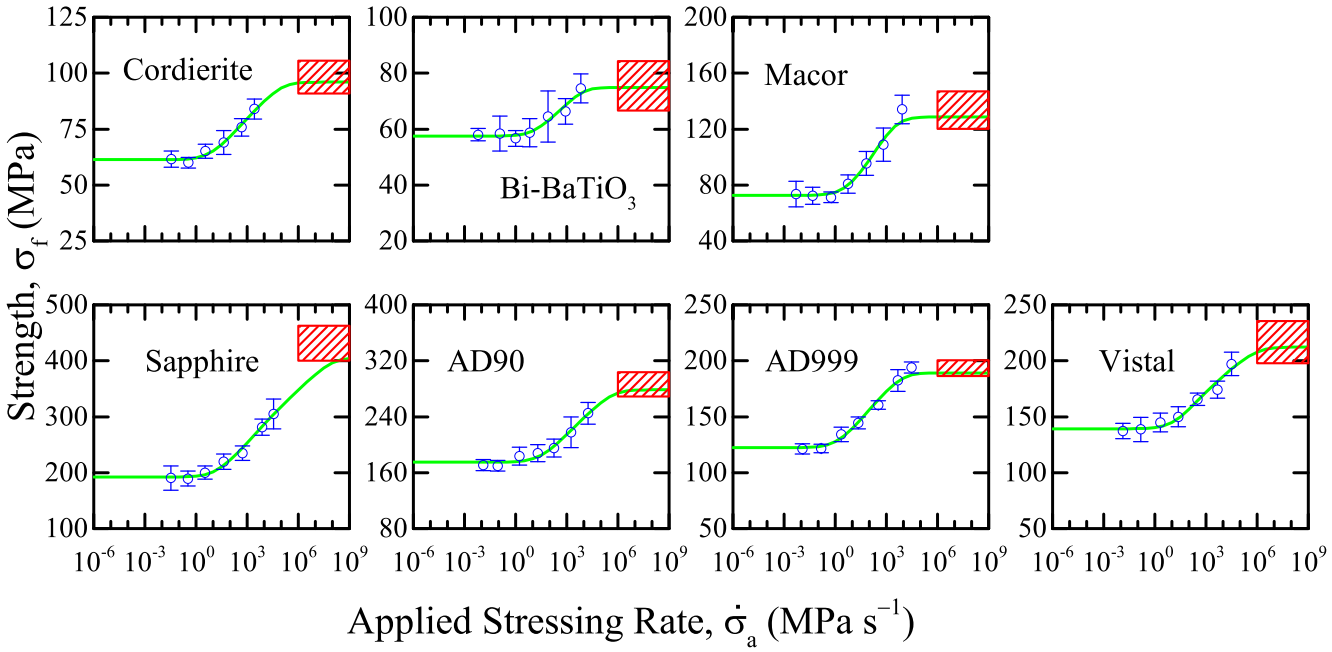

Fig. 6. Plots of the reactive strength responses for a range of ceramic materials. The solid lines represent best fits to the measurements using a combined meso-micro-nano-scale fracture model. The hatched boxes represent inert strengths.

Table II. Ceramic Crack Velocity and Reactive Fracture Properties

Material	Test indentation load, P (N)	Crack velocity parameters			Nano-scale reactive fracture parameters		
		η (J/m^2)	log (v_0/m s^{-1})	2γ (J/m^2)	a (Å)	u_0 (eV)	u_1 (eV)
Sapphire	3	1.00 ± 0.05	1.6 ± 0.1	5.8 ± 0.1	0.907	0.298	0.185
AD90	10	1.75 ± 0.05	2.6 ± 0.1	11.3 ± 0.1	0.686	0.332	0.118
AD999	100	1.35 ± 0.05	2.5 ± 0.1	4.1 ± 0.1	0.781	0.156	0.128
Vistal	100	0.70 ± 0.05	3.5 ± 0.1	0.50 ± 0.05	1.08	0.037	0.077
Cordierite	20	1.05 ± 0.05	3.0 ± 0.1	8.5 ± 0.1	0.885	0.416	0.102
Bi-$BaTiO_3$	5	0.35 ± 0.05	2.4 ± 0.1	3.8 ± 0.1	1.53	0.558	0.151
Macor	20	6.8 ± 0.1	3.8 ± 0.1	6.3 ± 0.1	0.348	0.048	0.030

increasing with stressing rate. Comparison of these strength-stressing rate combinations suggests that the fracture surfaces were beginning to react with the water environment in tens of milliseconds. The combined meso-micro-nano-scale model is able to describe the strengths over the complete reaction range, as noted by the solid line fits to the inert and reactive strengths, and contains three asymptotic responses: At very fast applied stressing rates, there is no time for the fracturing material to react with the environment and the strengths are invariant at the upper asymptote, σ_{max}, Eq. (13). At very slow applied stressing rates, there is adequate time for the fracturing material to completely react with the environment and the strengths are invariant at the lower asymptote, σ_{min}, Eq. (16). Intermediate to these two asymptotes, the fracturing material only has time to partially react with the environment and the strengths approach a near-logarithmic asymptote reflecting the reaction rate kinetics. Table II gives the parameters of η, v_0, and 2γ for each material describing the best fit solid lines of Fig. 6. The uncertainties given in Table II are the separations of the discrete values used in the matrix searching method. Comparison of Tables I and II shows that the ratio $2\gamma/2\gamma_0$ is approximately 0.3 for these oxide materials in water with the implication that T/T_0 is approximately 0.5.

IV. Applications of Multi-Length-Scale Models of Strength

In this section, six practical applications of the multi-scale strength analysis and experimental results of the previous two sections will be considered: three under inert conditions and three under reactive conditions. The final application considered, the prediction of reactive strengths, will be seen to provide experimental validation of the combined meso-micro-nano fracture model.

(1) Materials Design for Flaw Tolerance

Flaw tolerance is the ability of a component to retain its strength as flaws of increasing size are incorporated into the component. The indentation-strength measurements of Figs. 4 and 5 and the meso- and micro-scale strength analyses suggest there are two ways a ceramic materials designer might manipulate microstructure to achieve contact flaw tolerance, depending on the scale of the flaws. If flaw tolerance is required for large contact flaws, the material microstructure could be designed or manipulated such that the material is susceptible to lateral cracking or chipping. In this way, the residual stress field driving radial or half-penny cracks is reduced, that is K_r is reduced via Eq. (7), and the strengths approach the invariant minimum strength of σ_L, Eq. (8b). Physically, flaw tolerance is achieved by dissipating contact work through lateral cracking and the materials designer can quantify the flaw tolerance through measurement and reduction in P_L. Indentation observations suggest that materials with large E/H ratios are more susceptible to lateral cracking and chipping.[16] The trade-off in component performance is that achieving flaw tolerance in this way leads to greater surface wear and material removal.

If flaw tolerance is required for small contact flaws, the material microstructure could be manipulated such that the material is more susceptible to the formation of grain-localized crack wake restraints. In this case, the microstructural stress field that opposes crack opening is increased, that is the magnitude of K_μ is increased via Eq. (9), and the strengths approach the invariant maximum strength of σ_μ, Eq. (11b). Flaw tolerance is achieved here by dissipating the work of external loading by microstructural toughening, quantified by the measurement and increase in P^*. The trade-off in component performance in this case is that the design element must include reduced grain-boundary toughness, T_0, so as to enable the formation of ligamentary or frictional restraints, and hence flaw tolerance here is at the expense of overall decreased strengths.

If both meso- and micro-scale phenomena can be built into a material, such that P_L is small and P^* is large, flaw tolerance will be achieved for both large and small flaws. Such is the case for Vistal, shown in Fig. 5 and Table I. Over the same indentation load range, the strength of Vistal decreases by a factor of only two, compared with the factor of six for cordierite.

(2) Materials Selection

The explicit expression for inert strength covering the full indentation load range, Eq. (13), enables materials selection using strength distributions of components, once the distribution of contact loads a group of components will experience during their service life is specified. Given the probability density of contact loads, $dPr(P)/dP$, it is a simple matter to calculate the probability density of strengths, $dPr(\sigma_{max})/d\sigma_{max}$. For example, if there is a 10% chance that a component will experience a contact load between P_1 and P_2 during service, 10% of components will exhibit strengths between $\sigma_{max}(P_1)$ and $\sigma_{max}(P_2)$. Consider a group of components that will experience a normal distribution of contact loads over the service life, characterized by mean ± standard deviation. Figure 7(a) shows the probability densities of strengths that would result for the three polycrystalline Al_2O_3 materials for $P = (100 \pm 3)$ N using Eq. (13) and the parameters in Table I. The strength distributions are narrow, reflecting the relatively narrow load distribution, and the strength distributions are clearly separated. If no other factors were present then Vistal would be the choice for a structural application. However, if the application allowed for increase in size of a component, so as to achieve the same *load* carrying capacity using a smaller strength material, and cost was a factor, other materials might be better choices. In particular, AD90 might be a better choice if the cost/volume were approximately ¾ or less than that of Vistal. Figure 7(b) shows the probability densities of strengths that would result for a relatively broad load distribution $P = (10 \pm 3)$ N. All the strengths have increased as a consequence of the decreased flaw size, but only the Vistal material now exhibits a

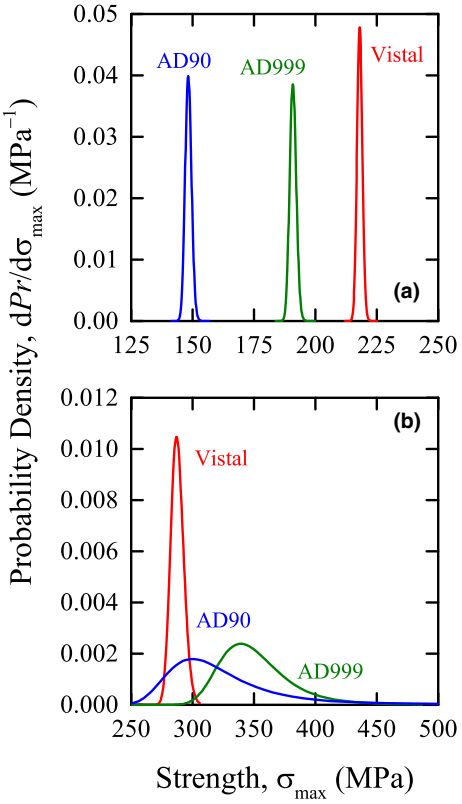

Fig. 7. Plots of predicted probability density strength distributions for three polycrystalline alumina materials. Indentation loads distributed normally with mean ± standard deviation of (a) (100 ± 3) N and (b) (10 ± 3) N.

relatively narrow strength distribution reflecting the flaw tolerance noted above. The AD999 and AD90 materials exhibit increasingly broad and asymmetric distributions reflecting the increasing lack of flaw tolerance and nonlinear dependence of strength on contact load. (The distributions are drawn in Fig. 7 such that the area under the curves is approximately equal.) In addition, the rank order of the strength distributions has changed from Fig. 7(a) and the distributions overlap. AD999 would now be the choice for structural applications, although the broad strength distribution would require significant margins of safety to be included in designs, thus driving up cost and weight. Other choices of the contact load distribution (*e.g.*, Poisson, bi-modal) will lead to changes in the predicted strength distributions and consequent changes in materials selection, but the measurements and fits of Fig. 5 provide the basis for selection of ceramic materials for structural applications in a quantitative manner.

(3) Toughness Curves and Intrinsic Strengths

Local to the crack tip, the equilibrium condition is given by (using Eq. 10)

$$K = K_a + K_r + K_\mu = T_0$$

In the far field, equilibrium is given by[8,9]

$$K_a + K_r = T_0 - K_\mu = T_0 + T_\mu, \tag{26a}$$

and the microstructural restraints appear as a crack-length-dependent toughening,

$$T_\mu(c) = -K_\mu(c) = \Delta T[1 - (\delta/c)^{3/2}] \tag{26b}$$

The variation of toughness with crack length, $T(c)$, is then given by

$$T(c)\begin{cases} = T_0, & c < \delta \\ = T_0 + T_\mu(c), & c \geq \delta \\ \rightarrow T_\infty, & c \gg \delta \end{cases} \tag{27}$$

$T(c)$ can be regarded as a property of the material and the "T-curve" can be used to predict the fracture behavior of the material under any external loading condition. Figure 8 shows the T-curves for four materials from Fig. 5 using Eqs. (26b) and (27) and values from Table I. Sapphire and the cordierite glass ceramic, neither of which exhibited effects of microstructure on fracture, have flat, invariant toughness responses. Conversely, the Vistal alumina and the Macor glass composite exhibit significant T-curves, reflecting the significant effects of microstructure on crack propagation in these materials. The comparison of Vistal with sapphire is particularly informative: For crack lengths less than about 40 μm, the toughness of Vistal is invariant and less than that of sapphire, reflecting the smaller toughness of the Vistal grain boundaries. For cracks longer than 40 μm, the Vistal toughness increases, surpassing that of sapphire for cracks about 80 μm long, reflecting the formation of increasing numbers of grain-localized restraints. For extremely long cracks, about 1000 μm long, the toughness of Vistal approaches the invariant steady-state toughness, considerably greater than that of sapphire.

A particularly useful application of T curves is the prediction of "intrinsic" strengths of components formed from materials such as Vistal and Macor in Fig. 8. Such strengths reflect the behavior when an indentation flaw is not deliberately introduced into a component. Setting $K_r = 0$ in Eq. (26a) is equivalent to setting $\tilde{P} = 0$in Eq. (13a) with the result that the predicted maximum strength is $\sigma^0_{max} = \sigma_\mu$ of Eq. (11b). Figure 9 shows a plot of measured intrinsic strengths, σ^i, of Macor, Vistal, and two other polycrystalline alumina materials[9,29,33] as a function of the values predicted in this way. The correlation is excellent as shown by the straight line indicating perfect agreement.

(4) Crack Velocity Curves

The fits of the reactive strength measurements shown in Fig. 6 and the resulting descriptive parameters given in Table II allow for direct comparison of the underlying crack velocity curves given by Eq. (20). Figure 10 compares the macroscopic crack velocity responses of Vistal, sapphire, and Macor using the (v_0, 2γ, η) values from Table II for straight cracks in components of 1 mm thickness. At a G value just

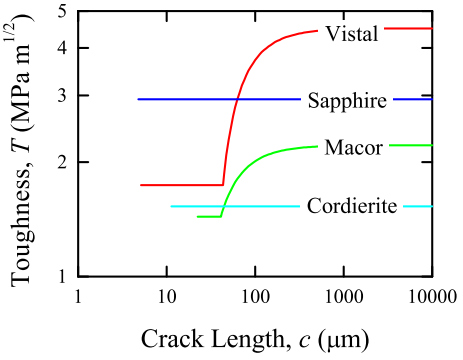

Fig. 8. Composite plot of the variation of toughness with crack length for four ceramic materials. Sapphire and Cordierite exhibit invariant toughness, whereas microstructural effects in Vistal and Macor lead to increasing toughness with crack length (T-curve behavior).

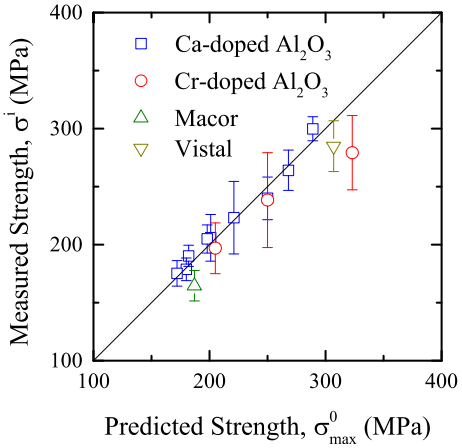

Fig. 9. Plot of measured intrinsic strengths *vs* those predicted from *T*-curve behavior for four ceramic materials. The symbols represent the means and standard deviations of at least 10 measurements for each material. The line represents exact agreement.

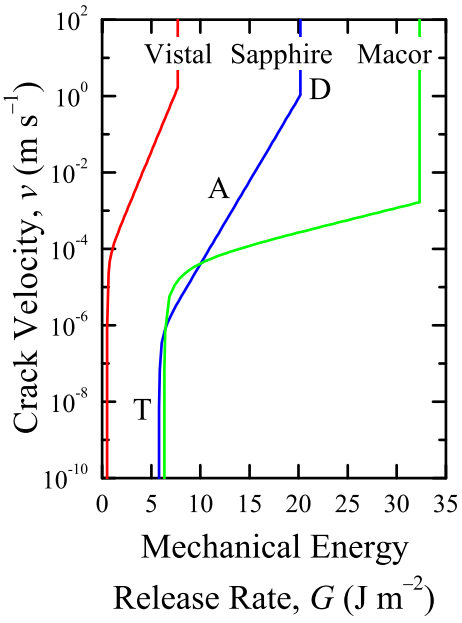

Fig. 10. Composite plot of the variation of crack velocity with mechanical energy release rate for three ceramic materials in water. The crack velocity thresholds are indicated by the rapid increase in velocity at the left of each response (marked T).

greater than the water crack velocity threshold value of $2\gamma = 5.8$ J/m^2, the crack velocity for sapphire in water increases significantly with negligible increase in G until a velocity of about 10^{-6} m/s is reached (marked region T). The velocity then increases exponentially with G (straight line in the semi-logarithmic coordinates), reflecting the mechanical activation of the nano-scale bond-breaking and reaction process (marked region A). At a G value of 20.2 J/m^2, representing the inert fracture resistance, the crack velocity increases dramatically with negligible increase in G, reflecting initial dynamic crack propagation in the absence of environmental effects (marked region D). (For crack velocities greater than those shown in Fig. 10, about 10% of the Rayleigh wave speed, dynamic effects dominate and $(G-2\gamma_0)$ ceases to be the sole measure of crack driving force.[8] Such effects have to be considered in crack propagation during inert strength tests.) The responses of Vistal and Macor are qualitatively the same, but Fig. 10 makes the quantitative similarities and differences readily apparent. Macor and sapphire have similar thresholds but very different activated responses, with Macor displaying a much weaker dependence on G and a much greater separation of the inert fracture resistance from the water threshold. These differences are a consequence of the very different chemistries of the two materials; in sapphire, Al–O bonds are rupturing and reacting with water and in Macor Si–O bonds are primarily rupturing and reacting. Conversely, sapphire and Vistal exhibit crack velocity curves of very similar shape, but the response of Vistal is translated to much smaller G values. In this case, it might be argued that the bond chemistry is similar, but the reduced water threshold and inert fracture resistance of Vistal reflect fracture of intergranular bonds compared with the fracture of transgranular bonds in sapphire. It is to be remembered that the $v(G)$ curves of Fig. 10 represent the synthesis of the meso-micro-nano fracture models, and hence the responses of Vistal and Macor represent the reactive fracture of the weak interfaces in these materials between the toughening bridging elements; in the case of Vistal these are grain boundaries.

(5) Bond Rupture Activation Barriers

The nano-scale parameters characterizing the discrete bond rupture energetics can be obtained by inversion of the relations, Eqs. (19–21), describing the macroscopic crack velocity:[10]

$$a = (2kT/\eta)^{1/2} \tag{28a}$$

$$u_0 = 2\gamma a^2 \tag{28b}$$

$$u_1 = kT\ln(2af_0/v_0) \tag{28c}$$

The values of these parameters for the seven materials in Fig. 6 are given in Table II, using the macroscopic crack velocity values listed, $T = 398$ K, and $f_0 = 3 \times 10^{14}$ Hz (calibrated by fitting Eq. (20) to the soda-lime glass measurements of Wiederhorn[30]). It is to be noted that the inferred parameters are indeed all nano-scale, of order Å (0.1 nm) for the physical length scale separating the energy barriers to bond rupture and of order eV (1.6×10^{-19} J) for the bond and barrier energies. These parameters can be used in Eq. (17) to explore how the bond rupture activation barriers vary as a crack extends during a reactive strength measurement.

Consider a straight edge crack, length c, in a sapphire plate of thickness w subjected to remote tension, σ_A. The crack area is then $A = wc$ and the SIF is simply K_a, Eq. (4). Using the Irwin relation, Eq. (15), allows the mechanical energy as a function of crack length to be calculated from $U_M = -\int G dA$. The total energy of the system as a function of crack length is then, using Eq. (17),[10]

$$\begin{aligned} U &= U_M + U_S \\ &= -(\psi^2\sigma_A^2 w/E)c^2 + u_0(wc/a^2) - (u_1/2)\cos(2\pi wc/a^2) \end{aligned} \tag{29}$$

Equation (29) is plotted in Fig. 11(a), using $w = 2$ mm, $\sigma_A = 400$ MPa, and the parameters for sapphire in water from Tables I and II. The variation is concave; there is an unstable equilibrium point at a crack length of about 10 μm. The variation also appears smooth at this scale, reflecting the continuum response at macroscopic dimensions, described by the first two terms in Eq. (29). If the axes are expanded, the discrete energy barriers, represented by the third term in Eq. (29), become apparent. Figure 11(b) shows an expanded view at the equilibrium point (corresponding to the point T in Fig. 10); the expansion is significant, about 10^4 horizontally and 10^{11} vertically. At this point, there is no net slope

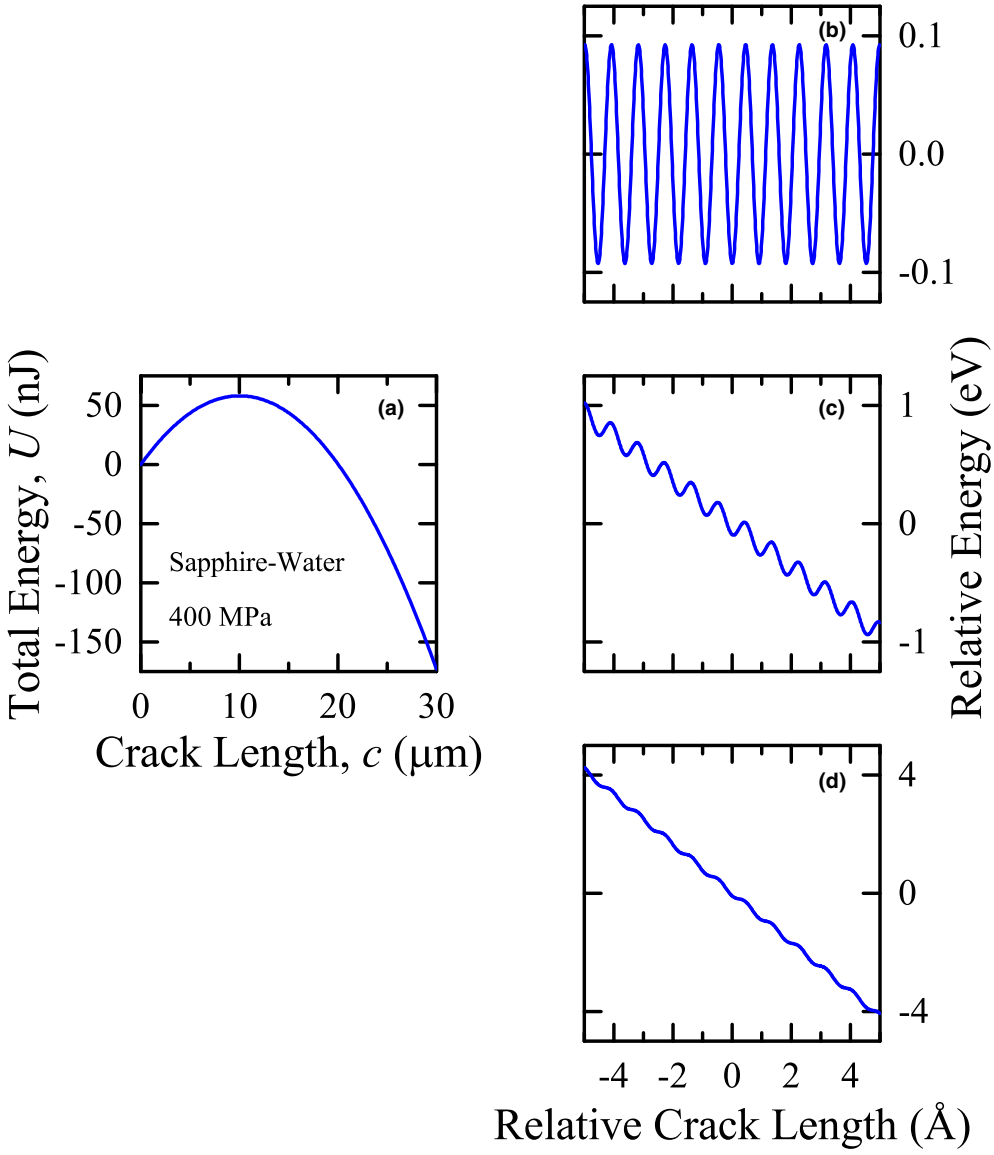

Fig. 11. Plots of the variation in energy with crack length for sapphire under applied stress in water. (a) Macroscopic continuum view exhibiting an unstable equilibrium at a crack length of about 10 μm. Nano-scale views exhibiting discrete barriers to bond rupture at crack lengths of (a) 10 μm, (b) 20 μm, and (c) 30 μm.

to the variation in energy, corresponding to equilibrium and the threshold in the macroscopic crack velocity response. The barriers for forwards and backwards bond rupture are equal such that there are equal numbers of bond rupturing and healing events along the crack front; the system is therefore in dynamic equilibrium and the crack is stationary. Figure 11(c) shows an expanded view at a crack length of about 20 μm (corresponding to the point A in Fig. 10). There is now a net slope to the energy variation corresponding to a nonequilibrium state. The increase in G associated with the increased crack length has mechanically activated the system such that the barriers to forward bond rupture are less than those for backward bond healing; averaged over the crack front there are more rupture events and the crack extends. Figure 11(d) shows an expanded view at a crack length of about 30 μm (corresponding to the point D in Fig. 10). The net slope now is so great that the energy barriers have all but disappeared; there is now practically no kinetic limitation on crack propagation and the crack propagates dynamically. The correspondence between the discrete nano-scale bond rupture behavior and the macroscopic crack velocity behavior has been noted (markings TAD). There is also a correspondence between the discrete behavior and the reactive strength responses: T corresponds to very slow applied stressing rates, A corresponds to intermediate rates, and D corresponds to very fast rates.

(6) Reactive Strength Predictions: Model Validation

The deconvolution of the inert strength responses via the combined micro-meso fracture model enabled the material properties of the underlying T curves to be determined, Fig. 8, and from these intrinsic strengths could be predicted, Fig. 9. Similarly, the deconvolution of the reactive strength responses via the combined meso-micro-nano fracture model enables the material properties of the underlying $v(G)$ curves to be determined, Fig. 10, and reactive strengths to be predicted. In particular, once the crack velocity parameters (v_0, 2γ, η) are determined using measurements at one indentation load, it is a simple matter to resolve the crack extension integral, Eq. (22), using different parameters in the mechanical energy release rate expression, Eq. (24), and the initial and final conditions, Eq. (25), to calculate the reactive strength response at a different indentation load. The Vistal and AD999 reactive strength responses in Fig. 6 were determined using an indentation load of $P = 100$ N, a load strongly affected by meso-scale flaw disruption and in a crack length range close to invariant steady-state micro-scale toughening

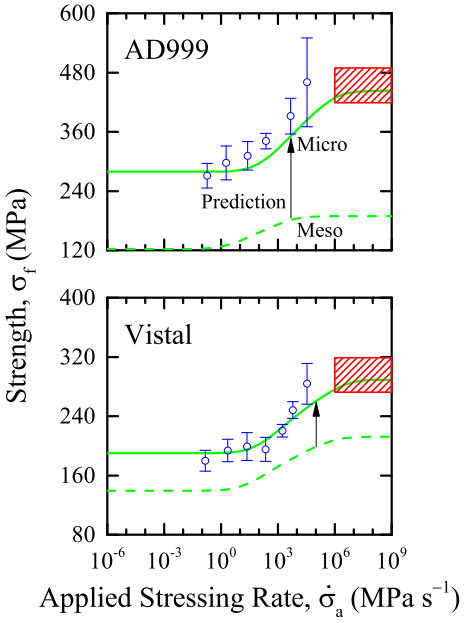

Fig. 12. Plots of the reactive strengths of AD999 and Vistal measured in the micro-scale range. The dashed lines represent best fits to measurements in the meso-scale range from Fig. 6. The solid lines are predictions for the strengths in the micro-scale range based on these measurements and assumed invariant nano-scale bond rupture mechanisms. The hatched boxes represent inert strengths.

effects. Figure 12 repeats as dashed lines the best fit reactive strength responses from Fig. 6 for these two materials at this indentation load. Also shown in Fig. 12 are *predicted* reactive strength responses for these two materials for an indentation load of $P = 3$ N, a load weakly affected by meso-scale flaw disruption and in a range in which micro-scale effects lead to large increases in toughness with crack length. Also shown in Fig. 12 as symbols are measured reactive strengths for these two materials using $P = 3$ N. There is very good agreement between these measurements performed in the micro range and the predictions from measurements performed in the meso range, with over a factor of 30 difference in contact load. Figure 12 highlights the engineering usefulness of the combined inert and reactive strength tests.

From a scientific point of view, the agreement between prediction and measurement in Fig. 12 provides validation for the multi-scale meso-micro-nano fracture model. Such validation provides support for the original contention that the nano-scale mechanisms of fracture are indeed separate from considerations of the larger scale fracture mechanics. Underpinning the predictions of Fig. 12 is the assumption that the $v(G)$ behavior of materials, for example, Fig. 10, is invariant with the crack size and the nature of the crack driving forces. The $v(G)$ behavior is a reflection of the bond rupture and reaction kinetics dictated by the energy barriers to rupture, for example, Fig. 11. The implication of the agreement in Fig. 12 is that these energy barriers, characterizing events local to the crack tip, although dependent on the net flux of energy to the tip via G, are indeed independent of the details of the mechanics characterizing crack loading given by $K(c)$. The large expansions of the axes required to observe the discrete bond rupture barriers in Fig. 11 further confirm that crack tips are "sharp" and that the mechanisms of crack propagation can be cleanly separated from the mechanics of fracture.

V. Conclusions

A unified multi-scale framework describes ceramic strengths very well: the framework relies on the separation of meso- and micro-scale mechanics of fracture from the nano-scale mechanisms of fracture. Mathematically, the framework is built on a description of the stress field in material adjacent to a crack tip by a SIF, treating the material as a linear-elastic continuum. The linearity enables SIFs from various loading sources, either driving or resisting crack propagation, to be added to arrive at a net SIF. Here, separate SIFs characterizing uniform applied stress, localized residual stress, and distributed restraining tractions were added to describe fracture during indentation-strength tests. The successful description of both inert and reactive strengths for a wide range of ceramics provides strong support for the application of the SIF in the multi-scale framework. The characteristic scales combined here were at the scale of the component (applied stress), the meso-scale of the indentation (residual stress), the micro-scale of the microstructure (restraining tractions), and the nano-scale of the crack tip, with attention focused on the meso-micro-nano synthesis.

If ceramic strengths are measured over a wide-enough range of indentation loads (several orders of magnitude) significant deviations from the ideal inert indentation-strength response are observed, providing insights into contact and fracture properties. Common to all ceramics is the increase in strength above the ideal response at large indentation loads, as meso-scale disruption of the indentation pattern by lateral cracking and chipping reduce the residual indentation stress field. For some ceramics, particularly those with coarse microstructures, there is a decrease in strength below the ideal response at small indentation loads, as micro-scale grain-localized crack restraints become less prevalent and the toughness of the material decreases. Both effects lead to flaw tolerance, in which strength decreases with increasing flaw size are diminished; lateral cracking is as effective as microstructural effects in this regard, providing some scope for materials designers. Both effects are well characterized by appropriate SIF-based models for indentation strength and the use of an effective indentation load allows the full strength range for all material responses to be described by a single meso-micro-scale analysis. The parameters extracted from the analysis can be used directly for strength predictions or to infer the variation of toughness with crack length. To avoid artifacts in the latter, meso-scale effects must be deconvoluted from the indentation-strength response to reveal underlying microstructural effects.

If ceramic strengths in reactive environments (here water) are measured over a large enough range of applied stressing rates (many orders of magnitude) it is clear that the strengths of all materials tend to invariant minimum values at slow rates. Such minimum strengths reflect thresholds in the underlying crack velocity functions and equilibrium surface states and energies of materials in reactive environments. Tests here suggest that such equilibria are achieved in about ten minutes for oxide ceramics in water. The full reactive strength range, between the minimum value and the conjugate maximum inert value, is well described by solution of a differential equation for crack extension based on nano-scale activated bond rupture. Required input parameters to the differential equation include parameters from the inert strength measurements, resulting in a combined meso-micro-nano analysis. Outputs from the combined analysis include macroscopic crack velocity parameters, including the all-important threshold, and nano-scale parameters characterizing the discrete energy barriers to bond rupture.

Both the inert strength variation with indentation load and the reactive strength variation with applied stressing rate are not simple power laws. In the first case, power-law behavior would derive from ideal indentation behavior, and in the second case, power-law behavior would derive from an assumed threshold-less empirical power-law crack velocity function. In both cases, increasing the experimental range of the controlled variable (load, rate) clearly revealed strength phenomena not encapsulated by power laws. Models for these phenomena based on simple physical principles were

developed in a straightforward manner. In the first case, a closed-form expression for the full strength range was developed and best fit to the full inert data set on a desk-top computer in minutes. In the second case, a differential equation for crack extension was developed, and the resulting computer-calculated failure stresses fit to the full reactive dataset in tens of minutes. A conclusion to be drawn from this is that there is no need to restrict analysis of indentation-strength measurements to ranges in which power laws appear to describe the data.

Finally, perhaps the most important aspect of this paper is shown in Fig. 12. In this figure, strengths at one indentation load are successfully predicted from measurements made at another load. The loads are separated across the meso-micro divide and have very different mechanics and yet both the reactive and inert measured strengths are in agreement with the predictions for both materials examined. The implication is that the underlying crack velocity function, reflecting nano-scale bond rupture mechanisms, is invariant with respect to changes in the fracture mechanics, quantified using SIFs determined by external boundary conditions. The invariance and quantitative agreement provide further support for the sharp crack tip as the basis for modeling fracture of ceramics.

Acknowledgments

The author thanks Dr. Brian Lawn for many years of stimulating discussion regarding fracture of ceramics and Dr. Michelle Oyen for much assistance and discussion regarding preparation of the Sosman Lecture and this manuscript. Any mention of commercial products is for information only; it does not imply recommendation or endorsement by NIST.

Panel A: Robert B. Sosman

Dr. Robert B. Sosman (1881–1967) was an experimental physical chemist who made "notable investigations in the theory and practice of the measurement of high temperatures." An extensive biography of Dr. Sosman's life is given in the Memorial by Austin,[34] including a bibliography of his published works. Dr. Sosman obtained a B.S. from the Ohio State University in 1903 and subsequently a Ph.D. from the Massachusetts Institute of Technology in 1907, the first year that the Institute had awarded a Ph.D.; Sosman was one of three, all chemists. After two years working with the consulting chemist Arthur D. Little in Boston, in 1908 Dr. Sosman joined the Geophysical Laboratory of the Carnegie Institution of Washington, DC with Arthur L. Day as Director. From a measurements and standards perspective, it was here that Sosman made one of his earliest contributions with the publication with Day in 1911 of *High Temperature Gas Thermometry*, which described the development of a nitrogen gas temperature scale that extended to 1550°C. The results of this comprehensive and extremely thorough work were included in the first International Temperature Scale, ITS-27, adopted by the international standards community in 1927, and in its successor, ITS-48, in 1948. Thoroughness and high temperature investigations were to be hallmarks of Dr. Sosman's career. World War I led to the Geophysical Laboratory performing research on glass production and it was in this that Sosman developed an interest in refractories and in the various forms of silica, the latter of which he is probably best known in the ceramics community. In 1928, Sosman joined the Research Laboratory of the U.S. Steel Corporation in Kearny, NJ, rising to become Assistant Director of the Laboratory in 1944. In 1947, Sosman retired from US Steel and became a Visiting Professor in the Department of Ceramics at Rutgers University in New Brunswick, NJ, where he was encountered by the last Sosman awardee to be taught by Dr. Sosman himself, Prof. A.H. Heuer.[35] In 1962, Sosman became Professor Emeritus.

Dr. Sosman served as President of the American Ceramic Society in 1937-1938 and was recognized by the Society for his research contributions by the Edward Orton Jr Memorial Lecture in 1937, the Alfred V. Bleininger Award in 1953, the Ross Coffin Purdy Award in 1957, and the John Jeppson Medal in 1960. In a newspaper article recognizing his Bleininger Award, the Westfield (NJ) Leader, January 29, 1953, highlighted Sosman's long interest in minerals, ceramics, and high temperatures by noting that "As a youngster, Dr. Sosman got a first glimmering of science when he decided one day to build a miniature blast furnace in the yard of his home in Chillicothe, Ohio." The Leader noted that although Sosman had plenty of iron ore, his furnace produced no metal.

Dr. Sosman was a prolific writer, publishing over 80 works from between 1905 and 1965. Chief amongst these were two large works concerning silica: *The Properties of Silica. An Introduction to the Properties of Substances in the Solid Non-Conducting State*, 1927 (856pp.)[36] and *The Phases of Silica*, 1965 (399pp.),[37] which was a revision of the first 14 chapters of the earlier work. There is no doubt that Sosman's thoroughness in these works was a little unnerving to his contemporaries. In a review of *The Properties of Silica* in 1929, the reviewer Lowry[38] writes "The book is made more formidable by the author's anxiety to use a logical method of classifying data, since he threatens in his introductory chapter to write a book of 57 chapters, to deal with all possible combinations of the six fundamental concepts of length, time, mass, electric charge, entropy, and energy, …". Austin refers to it as an "exhaustive treatise." Sosman's energy and enthusiasm for the subject is evidenced by the fact that he began the revision to this work when he became an Emeritus Professor at the age of 81, 35 yr after the original publication. Here again, a 1966 reviewer Zussman[39] notes Sosman's comprehensive approach in *The Phases of Silica*: "… the author describes the nature and interrelations between the various phases of silica. His interpretation of the term phases allows him to recognize 22 of them, not including melanophlogite which Sosman regards as of doubtful validity. … Alternative usage of the term phase would recognize only 11 silicas even if melanophlogite were included."

On the nontechnical side, Sosman also exhibited energy. He was the seventh person to hike the entire length of the Appalachian Trail from Maine to Georgia. He was an enthusiastic dancer and diner, and here again his drive for classification and order was apparent. Sosman was an enthusiastic explorer of the different restaurants of Manhattan, and collected data on the restaurants he visited. From 1942 to 1962, he published these data privately, in the form of handbooks, for friends, entitled *Gustavademecum for the Island of Manhattan* (*gustavademecum*, Latin for "taster's manual"). The handbook included information on the type, cost, and quality of food in each restaurant, the illumination, and the quality of the patrons and waiters. Being Sosman, the restaurants were arranged in order of increasing latitude and longitude.

References

[1]M. P. Harmer, "Interfacial Kinetic Engineering: How Far Have We Come Since Kingery's Inuagural Sosman Address," *J. Am. Ceram. Soc.*, **93** [2] 301–17 (2010).

[2]W. D. Kingery, "Plausible Concepts Necessary and Sufficient for the Interpretation of Ceramic Grain-Boundary Phenomenon: I, Grain-Boundary Characteristics, Structure, and Electrostatic Potential," *J. Am. Ceram. Soc.*, **57** [1] 1–8 (1974).

[3]B. R. Lawn, "Physics of Fracture," *J. Am. Ceram. Soc.*, **66** [2] 83–91 (1983).

[4]B. J. Hockey and B. R. Lawn, "Electron Microscopy of Microcracking About Indentations in Aluminium Oxide and Silicon Carbide," *J. Mater. Sci.*, **10** [8] 1275–84 (1975).

[5]B. R. Lawn, B. J. Hockey, and S. M. Wiederhorn, "Atomically Sharp Cracks in Brittle Solids: An Electron Microscopy Study," *J. Mater. Sci.*, **15** [5] 1207–23 (1980).
[6]J. E. Sinclair and B. R. Lawn, "An Atomistic Study of Cracks in Diamond-Structure Crystals," *Proc. Roy. Soc. Lond. A*, **329** [1576] 83–103 (1972).
[7]J. Thurn and R. F. Cook, "The Effects of Inter-Surface Cohesive Forces on Linear and Penny-Shaped Cracks," *Inter. J. Fracture*, **119** [2] 103–24 (2003).
[8]B. R. Lawn, *Fracture of Brittle Solids-Second Edition*. Cambridge University Press, Cambridge, 1993.
[9]R. F. Cook, E. G. Liniger, R. W. Steinbrech, and F. Deuerler, "Sigmoidal Indentation-Strength Characteristics of Polycrystalline Alumina," *J. Am. Ceram. Soc.*, **77** [2] 303–14 (1994).
[10]R. F. Cook, "Environmentally-Controlled Non-Equilibrium Crack Propagation in Ceramics," *Mater. Sci. Eng., A*, **260** [1–2] 29–40 (1999).
[11]R. F. Cook, B. R. Lawn, and C. J. Fairbanks, "Microstructure-Strength Properties in Ceramics: I-Effect of Crack Size on Toughness," *J. Am. Ceram. Soc.*, **68** [11] 604–15 (1985).
[12]R. F. Cook, B. R. Lawn, and C. J. Fairbanks, "Microstructure-Strength Properties in Ceramics: II-Fatigue Relations," *J. Am. Ceram. Soc.*, **68** [11] 616–23 (1985).
[13]R. F. Cook, "Crack Propagation Thresholds: A Measure of Surface Energy," *J. Mater. Res.*, **1** [6] 852–60 (1986).
[14]R. F. Cook, "Toughening of a Cordierite Glass-Ceramic by Compressive Surface Layers," *J. Am. Ceram. Soc.*, **88** [10] 2798–808 (2005).
[15]B. R. Lawn, A. G. Evans, and D. B. Marshall, "Elastic/Plastic Indentation Damage in Ceramics: The Median/Radial System," *J. Am. Ceram. Soc.*, **63** [9–10] 574–81 (1980).
[16]R. F. Cook and G. M. Pharr, "Direct Observation and Analysis of Indentation Cracking in Glasses and Ceramics," *J. Am. Ceram. Soc.*, **73** [4] 787–817 (1990).
[17]B. R. Lawn and A. G. Evans, "A Model for Crack Initiation in Elastic/Plastic Indentation Fields," *J. Mater. Sci.*, **12** [11] 2195–9 (1977).
[18]Y. Murakami, et al. (eds.), *Stress Intensity Factors Handbook*, p. 669. Pergamon Press, Oxford, 1987.
[19]G. R. Anstis, P. Chantikul, D. B. Marshall, and B. R. Lawn, "A Critical Evaluation of Indentation Techniques for Measuring Fracture Toughness: I. Direct Crack Measurements," *J. Am. Ceram. Soc.*, **64** [9] 533–8 (1981).
[20]P. Chantikul, G. R. Anstis, D. B. Marshall, and B. R. Lawn, "A Critical Evaluation of Indentation Techniques for Measuring Fracture Toughness: II. Strength Method," *J. Am. Ceram. Soc.*, **64** [9] 529–43 (1981).
[21]D. B. Marshall, B. R. Lawn, and A. G. Evans, "Elastic/Plastic Indentation Damage in Ceramics: The Lateral Crack System," *J. Am. Ceram. Soc.*, **65** [11] 561–6 (1982).
[22]R. F. Cook and D. H. Roach, "The Effect of Lateral Crack Growth on the Strength of Contact Flaws in Brittle Materials," *J. Mat. Res.*, **1** [4] 589–600 (1986).
[23]W. D. Kingery, H. K. Bowen, and D. R. Uhlmann, *Introduction to Ceramics-Second Edition*. Wiley Interscience, New York City, New York, 1976.
[24]R. Knehans and R. Steinbrech, "Memory Effect of Crack Resistance During Slow Crack Growth in Notched Al_2O_3 Bend Specimens," *J. Mater. Sci. Lett.*, **1** [8] 327–9 (1982).
[25]M. V. Swain, "R-Curve Behavior in a Polycrystalline Alumina Material," *J. Mater. Sci. Lett.*, **5** [12] 1313–5 (1986).
[26]S. J. Bennison and B. R. Lawn, "Role of Interfacial Grain-Bridging Sliding Friction in the Crack-Resistance and Strength Properties of Nontransforming Ceramics," *Acta Metall.*, **37** [10] 2659–71 (1989).
[27]P. Chantikul, S. J. Bennison, and B. R. Lawn, "Role of Grain Size in the Strength and R-Curve Properties of Alumina," *J. Am. Ceram. Soc.*, **73** [8] 2419–27 (1990).
[28]J. E. Blendell and R. L. Coble, "Measurement of Stress Due to Thermal Expansion Anisotropy in Al_2O_3," *J. Am. Ceram. Soc.*, **65** [3] 174–8 (1982).
[29]R. F. Cook, "Segregation Effects in the Fracture of Brittle Materials: Ca-Al_2O_3," *Acta Metall.*, **38** [6] 1083–100 (1990).
[30]S. M. Wiederhron and L. H. Bolz, "Stress Corrosion and Static Fatigue of Glass," *J. Am. Ceram. Soc.*, **53** [10] 543–8 (1970).
[31]J. R. Rice, "Thermodynamics of the Quasi-Static Growth of Griffith Cracks," *J. Mech. Phys. Solids*, **26** [2] 61–78 (1978).
[32]R. F. Cook and E. G. Liniger, "Kinetics of Indentation Cracking in Glass," *J. Am. Ceram. Soc.*, **76** [5] 1096–106 (1993).
[33]R. F. Cook, C. J. Fairbanks, B. R. Lawn, and Y.-W. Mai, "Crack Resistance by Interfacial Bridging: Its Role in Determining Strength Characteristics," *J. Mat. Res.*, **2**, 345–56 (1987).
[34]J. B. Austin, "Memorial to Robert Browning Sosman (1881–1967)," *Proc. Vol. Geol. Soc. Am.*, 251–8 (1968).
[35]A. H. Heuer, "Robert B. Sosman Remembered," *Ceram. Bulletin*, **65** [7] 1034 (1986).
[36]R. B. Sosman, *The Properties of Silica*. Book Department, The Chemical Catalog Company, Inc., New York City, New York, 1927.
[37]R. B. Sosman, *The Phases of Silica*. Rutgers University Press, New Brunswick, 1965.
[38]T. M. Lowry, "The Properties of Silica," *Nature*, **123** [3091] 122–3 (1929).
[39]J. Zussman, "The Phases of Silica"; International Union of Crystallography, Book Reviews. http://journals.iucr.org/q/issues/1966/07/00/a05203/a05203.pdf, Accessed 4/15/2015. □

Robert F. Cook is a Fellow at the National Institute of Standards and Technology (NIST), Gaithersburg, MD. Dr. Cook received a B.Sc. (First Class Honors) in Physics from Monash University, 1981, and a Ph.D. in Physics from the University of New South Wales, 1986. At NIST, he was Leader of the Nanomechanical Properties Group and Deputy Chief of the Ceramics Division, 2005–2011, prior to his appointment as Fellow in 2011. Dr. Cook was a Professor at the University of Minnesota, 1998–2004, and a Research Staff Member at IBM Research, 1985–1998. Dr. Cook has authored over 160 archival publications and holds 14 patents; his primary field of research is the mechanical properties of materials, especially fracture. Dr. Cook has received Department of Commerce Silver and Bronze medals for his research on nanoparticles and scanning probe microscopy. Dr. Cook was Chair of the Basic Science Division of ACerS, 2002–2003, and served on the ACerS Board of Directors, 2004–2007; he received the Robert B. Sosman Award, 2014, the Richard M. Fulrath Award, 1999, and was elected an ACerS Fellow in 1998. Dr. Cook's current research is on the development of measurement methods and standards for mechanical properties of materials at ultra-small scales.